J Appl Electrochem (2009) 39:1425–1436
DOI 10.1007/s10800-009-9819-0

ORIGINAL PAPER

Effect of a net on the limiting current distribution in a parallel plate electrochemical reactor: part I. Individual effects

Murali Venkatraman · J. W. Van Zee

Received: 9 October 2006 / Accepted: 29 January 2009 / Published online: 13 February 2009

Abstract In some aqueous-metal batteries or electrochemical parallel plate reactors, the spacing between the electrodes is controlled by a porous net. This net affects the limiting current distribution because it disrupts the parabolic laminar flow velocity distribution. Here, computational fluid dynamics (CFD) is used to solve the Navier-Stokes equations surrounding the inert net and the effect of the net geometry on the limiting current density is studied. The location, spacing, and number of the longitudinal and transverse ribs of the net are shown to affect the local and average current density distributions on each of the two electrodes. The effect of transverse ribs on the current distribution was found to be much higher than the longitudinal ribs. The results show that the longitudinal ribs decrease the local current density at the electrode which is not in contact and increase the current density the space between two adjacent longitudinal ribs at the electrode in contact. The transverse ribs on the other hand, increase the local current density to very high values at the electrode that is not in contact. The current density, however, falls along the flow direction as it exits the transverse-ribs region. These effects were observed to be mainly due to the changes in flow field distribution. A deviation of −40% was observed for a system of 4 longitudinal ribs and no transverse ribs at the non-dimensional axial position 0.06. For 2 transverse ribs, the deviation at the same axial position was approximately 250% of the local current density. All the results are for a net with a spacing of 0.94×10^{-3} m.

Keywords Enhancement factor · Limiting current · Longitudinal and transverse ribs · Nusselt number distribution · Obstructed channel flow

List of symbols

C	Local concentration (kmol m^{-3})
C_b	Bulk concentration (kmol m^{-3})
C_{in}	Inlet concentration (kmol m^{-3})
C_s	Wall or surface concentration (kmol m^{-3})
D	Diffusion coefficient of OH^- ion (m^2 s^{-1})
h	Local heat transfer coefficient (W m^{-2} K^{-1})
h_1	Thickness of transverse rib in z direction (m)
h_2	Thickness of longitudinal rib in z direction (m)
i	Local current density (A m^{-2})
i_{avg}	Plate-average current density (A m^{-2})
$i_{avg\text{-}noribs}$	Plate-average current density for no-ribs case(A m^{-2})
i^*	Normalized local current density (dimensionless)
$\hat{i}$	local current density averaged over η direction (A m^{-2})
$\hat{i}^*$	Normalized local current density averaged over η direction (dimensionless)
k_m	Mass transfer coefficient (m s^{-1})
L	Electrode length in y direction (m)
l	Equivalent diameter (m)
l_1	Live cell spacing in x direction (m)
l_2	Live cell spacing in y direction (m)
n_l	Number of longitudinal ribs
n_t	Number of transverse ribs
Nu	Local Nusselt number (dimensionless)

M. Venkatraman (✉) · J. W. Van Zee
Department of Chemical Engineering, University of South Carolina, Columbia 29208, USA
e-mail: Murali.Venkatraman@csiro.au

Present Address:
M. Venkatraman
CSIRO Materials Science and Engineering, Private Bag 33, Clayton South MDC, VIC 3169, Australia

Nu_{avg}	Plate-average Nusselt number (dimensionless)
$\hat{N}u$	Local Nusselt number averaged over η direction
Pr	Prandtl number
Re	Reynolds number based on the equivalent diameter
Sc	Schmidt number
W	Electrode width in x direction (m)
w_1	Width of the longitudinal rib in x direction (m)
w_2	Width of the transverse rib in y direction (m)
$\bar{v}$	Average velocity (m s^{-1})

Greek symbols

Δ	Deviation factor (dimensionless)
$\hat{\Delta}$	Deviation factor averaged over η direction (dimensionless)
η	Non-dimensional x coordinate
ζ	Non-dimensional y coordinate
μ	Molecular viscosity (Pa s)
Θ	Dimensionless concentration (Eq. 9)

Subscripts

1	Electrode 1
2	Electrode 2
avg	Average
avg_noribs	Average for the no-ribs case

Superscripts

*	Dimensionless quantity obtained by dividing the respective quantity by its average
^	Dimensionless quantity averaged in x or η direction

1 Introduction

Parallel plate electrochemical reactors (PPERs) are used in chlor-alkali production, metal extraction and refining as well as in batteries and fuel cells and their design often requires predicting quantities such as current density distribution, energy efficiency, conversion per pass of a reactant or product, and selectivity of a desired product. Two-dimensional models have been discussed [1–7]. Most of these models feature infinitely wide electrodes where edge effects are absent, velocity profiles obtained from analytical solutions to the Navier-Stokes equations, and numerical solution of the model equations was based on the finite-difference technique developed by Newman [8] or one of its modifications (e.g. see Ref [9]). Here we consider an extension of these channel and PPER models for the case when a porous net separates the electrodes (see Fig. 1).

The need for this net arises in semi-fuel cells (SFCs) or metal-aqueous batteries [10–14] where it is desirable to maintain the minimum gap or pitch between the electrodes. The net is inert and limiting current analyses based on existing models for obstacles in the flow field for both laminar and turbulent flow, reported in the literature [15–21], provide some perspective albeit not one that is readily applicable to our case. As a first step toward understanding of these net-based PPERs, we consider the limiting current density analysis based on the solution to the closely associated heat-transfer problem [22, 23].

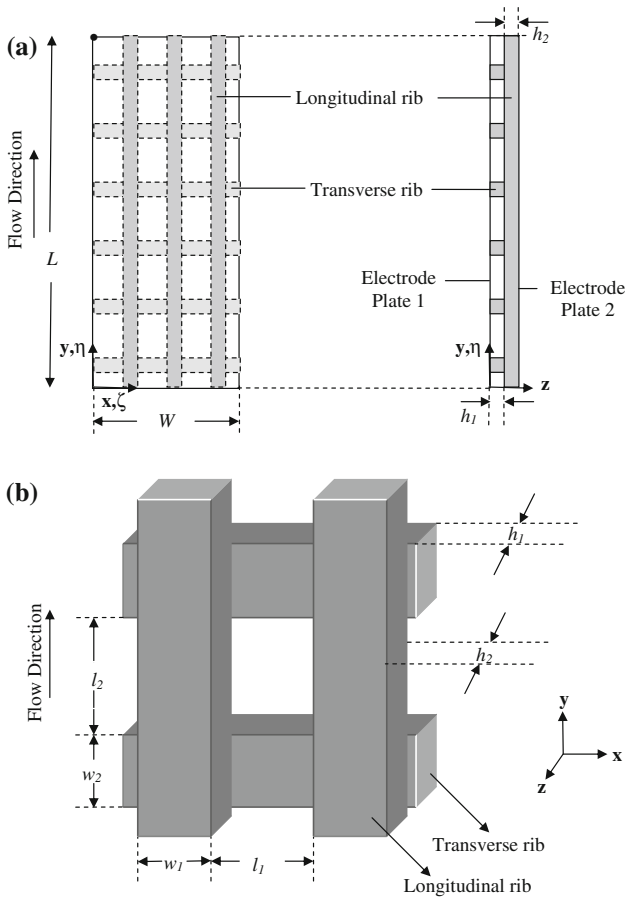

Fig. 1 **a** Schematic of two parallel plate electrodes with an inert net between them. The flow is fully developed and laminar with the electrochemical reactions occurring at the electrodes under limiting current conditions. The dotted lines in **(a)** show the net with the transverse and longitudinal ribs, in between the electrode plates. **b** Structure of the inert net employed in this study Refer to Table 1 for the values of the various dimensions used

2 Mathematical model

Figure 1 shows a schematic of two parallel-plate electrodes with an inert net in between. The electrolyte enters through a diffuser (not shown) at a constant velocity 0.01 m s^{-1}, and the free stream velocity is well established prior to contacting the inert net. Dilute species within the fluid are reacted electrochemically without gas evolution at the electrodes and the bulk electrolyte exits the net section of

the PPER at a length, L, and flows into an exit diffuser so that the velocity at L is not disturbed. In an actual SFC, an active metal anode (Al, Mg or Li) [13], alkaline electrolyte (NaOH + H_2O_2) and a noble metal cathode (Ag, Ni, Pt or Pd) [24] are used. The electrodes may dissolve [25] during the operation but to prevent loosening of the configuration during the dissolution, a constant pressure is applied on the back of the electrodes. No shape changes associated with this dissolution are considered.

The net is made of an impervious plastic and has a layered structure (see Fig. 1b). The net is not interwoven, but consists of two layers of plastic ribs—transverse and longitudinal—pressed on each other. In Fig. 1 h_1 and h_2 are the heights of the ribs; l_1 and l_2 are the live cell spacing in the two layers; w_1 and w_2 are the widths of the two layers. Table 1 provides all the dimensions. Note that we label the region where the fluid is present as a "live cell".

The current approach could be used for a mesh corresponding to an interwoven geometry but the computational grid would be very different from that presented in Figs. 1, 2 and needs to be constructed separately. The results will be different because from one perspective the interwoven grid will decrease the flow area by a factor of 2 in a triangular geometry. In addition, the symmetry will be elongated over two ribs (adjacently placed). This applies both to the longitudinal and transverse ribs. Also, the effects of local curvature and non-rectangular cross sections may have to be included in the computations.

We use the previously computed distribution of the Nusselt number [23] and the analogy between heat and mass transfer [26]. In an aluminum anode the surface reaction results in a layer of alumina [10, 25], which drives the anode to be mass-transfer controlled by the transport of OH^- ions. At the cathode, the reduction of H_2O_2 takes place, which is limited by the transport of HO_2^- ions [24]. Thus at high current densities, the SFC may operate under mass transfer limitations and the current density is related to the flux of the ion as follows [8]:

Table 1 Dimensions

Dimensions	Value (m)
L	72×10^{-3}
W	37×10^{-3}
h_1	0.27×10^{-3}
h_2	0.27×10^{-3}
l_1	1.54×10^{-3}
l_2	1.54×10^{-3}
w_1	0.94×10^{-3}
w_2	0.94×10^{-3}

$$\left|\frac{\mathrm{i}}{n\mathrm{F}}\right| = k_m(C_b - C_s) \tag{1}$$

where the local mass transfer coefficient k_m is :

$$k_m = \frac{-D}{C_b - C_s}\left(\frac{\partial C}{\partial z}\right)_{z=z_s} \tag{2}$$

where s denotes surface. The Nusselt number Nu is given by:

$$Nu = \frac{k_m l}{D} \tag{3}$$

At limiting current conditions, the surface concentration C_s goes to zero and the distribution of the current density is given by:

$$|\mathrm{i}| = n\mathrm{F}C_b\left(\frac{D}{l}\right)Nu \tag{4}$$

The average current density is given by:

$$\left|\mathrm{i}_{avg}\right| = \left|\frac{1}{A}\int_A \mathrm{i}.dA\right| = \left(\frac{n\mathrm{F}D}{l}\right)\frac{1}{A}\int_A (C_b Nu)dA \tag{5}$$

where A is the area of the electrode.

Typically, we are interested in calculating the average current density of the individual electrodes and identifying the regions of the reactor where the current density is above or below average to understand the reaction distribution so that the system can be designed with optimum amount of material, minimum costs and maximum energy efficiency. By normalizing the local current density i against the respective electrode average current density i_{avg} we eliminate the dependence on number of electrons n transferred at a given electrode, diffusivity of the limiting ion D and also the model shape factor l, (i.e. the number of ribs for a given geometry) The cathodic currents are negative and anodic currents are positive [8]. Hence $\frac{|i|}{|i_{avg}|}$ is the same as $\frac{i}{i_{avg}}$ which is the normalized current density denoted by i^*. i_1^* and i_2^* can be used as measures to understand the performance of electrodes 1 and 2 respectively.

In a PPER with no obstacles in the flow path the entire surface area of the electrode is in contact with the electrolyte solution and calculating average current density for a single reaction is straightforward. In SFCs, part of the electrode is hidden from the electrolyte by the ribs of the net (see Fig. 1) and such areas are unavailable for electrochemical reaction. Hence, there is a choice between the geometrical plate area A_{noribs} and the area available for mass transfer A for calculating average current density. Also, depending on the electrode, only one kind of rib (transverse or longitudinal) presses against an electrode. Hence there are two different electrode areas A_1*and* A_2, available for normalizing the

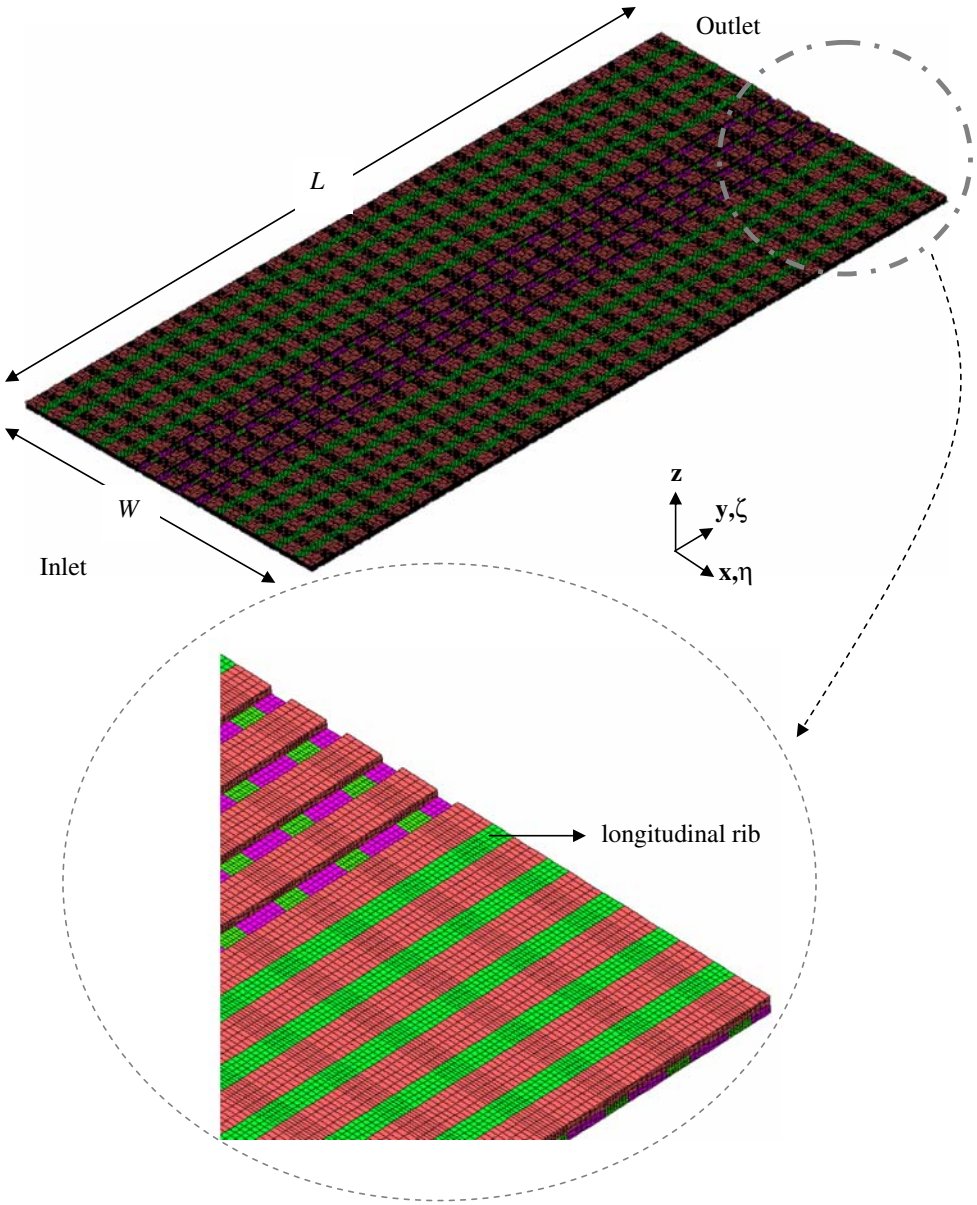

Fig. 2 Schematic of a typical computational mesh (exploded view in the encircled figure) used in this work showing no-ribs in the center and 5 longitudinal ribs on either side. Note that a maximum of equally spaced 14 longitudinal and 29 transverse ribs were used in the study

individual electrode current densities i_1 and i_2. A_1 *and* A_2 are linearly related to the geometric plate area A_{noribs} through simple algebraic expressions involving the number of longitudinal and transverse ribs n_l and n_t respectively.

$$A_1 = A_{noribs} - n_t(w_2 W) \tag{6}$$

$$A_2 = A_{noribs} - n_l(w_1 L) \tag{7}$$

We refer to both as A in the ensuing discussions. The geometric plate area is labeled A_{noribs}. All calculations for i_{avg} have been based on A_1*and* A_2. The current density may be adjusted to $A_{noribs}$by using Eq. 6 and 7. We present the normalized current (i.e. Eq. 5) regardless of the number of ribs and discuss in Part II the enhancement of the average current density based on A_{noribs}.

Two cases occur during the evaluation of the integral in Eq. 5: (1) C_b is a constant along the flow direction which is applicable for situations where conversion is low (<3%) (2) where C_b is not constant. Case 1 corresponds to the Lévêque solution of the Graetz problem [27] and case 2 corresponds to the complete Graetz solution. For the problem under consideration, the PPER is long enough and the conversion was approximately 30%. i in Eq. 4 is calculated based on C_b, and C_b is obtained by averaging C in the z direction from one electrode plate to the other [26] :

$$C_b(x,y) = \frac{\int_0^{h_1+h_2} v(x,y,z)\cdot C(x,y,z)dz}{\int_0^{h_1+h_2} v(x,y,z)dz} \tag{8}$$

We further simplify the definition of i^* by defining a dimensionless concentration Θ[8]:

$$\Theta = \left| \frac{C - C_s}{C_{in} - C_s} \right| \tag{9}$$

so that at limiting current conditions when $C_s = 0$,

$$C_b = C_{in}\Theta_b \tag{10}$$

Substituting, we get:

$$i^* = \frac{(\Theta_b Nu)}{\frac{1}{A}\int_A (\Theta_b Nu)dA} \tag{11}$$

In this work, the reference taken is the no-ribs case with fully-developed, laminar flow of a Newtonian liquid with constant properties, between the two flat electrode plates, with no obstacles present in the flow-field path. The correlation and discussion for this can be obtained from our previous work [23]. We use the afore-mentioned correlation along with Eq. 11 to establish the no-ribs case in Fig. 3. We introduce a new quantity $\hat{i}$ which denotes the current density averaged across the plate, in a direction η perpendicular to the primary flow direction ζ. Thus,

$$\hat{i} = \int_0^{\frac{W}{L}} |i| d\eta \tag{12}$$

and when $\hat{i}$ is normalized against i_{avg}, it is related to Nu as :

$$\hat{i}^* = \frac{\hat{i}}{i_{avg}} = \frac{\left(\hat{\Theta}_b \hat{N}u\right)}{\frac{1}{A}\int_A (\Theta_b Nu)dA} \tag{13}$$

where $\hat{\Theta}_b$ and $\hat{N}u$ have meanings similar to $\hat{i}$. We denote Δ as the deviation of current density from the numerically calculated no-ribs case, at any point in the plates, and define it as follows:

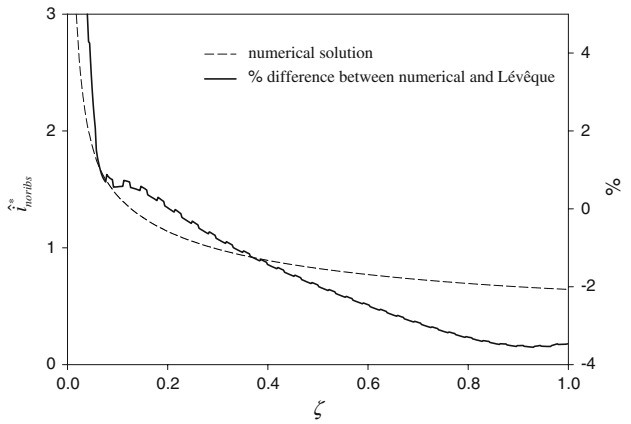

Fig. 3 Predicted variation of normalized local average limiting current density $\hat{i}^*_{noribs}$ along the flow direction ζ, based on the mass transfer correlation for the unobstructed channel with laminar flow, for a Newtonian liquid with constant properties. No longitudinal or transverse ribs are present in this case. Also shown is the % difference between the numerical solution and the theoretical Lévêque solution

$$\Delta = \frac{i - i_{noribs}}{i_{avg\_noribs}} \tag{14}$$

This simplifies as:

$$\Delta = \left(\frac{i_{avg}}{i_{avg\_noribs}}\right) i^* - i^*_{noribs} \tag{15}$$

where Δ is a function of η and ζ. The effects of transverse and longitudinal cases are quantified as deviation from the no-ribs case using Δ. $i^*$and $i^*_{noribs}$are given by Eq. 11 and to evaluate $\left(\frac{i_{avg}}{i_{avg\_noribs}}\right)$ we use the definition of the average current densities for ribbed and non-ribbed cases (see Eq. 5):

$$\frac{i_{avg}}{i_{avg\_noribs}} = \left(\frac{l_{noribs}}{l}\right) \frac{\frac{1}{A}\int_A (\Theta_b Nu)dA}{\frac{1}{A_{noribs}}\int_A (\Theta_{b_{noribs}} Nu_{noribs})dA} \tag{16}$$

3 Numerical procedure

A commercially available CFD solver (STAR-CD v3.15) was used to calculate the Nu distribution for the geometry given in Figs. 1, 2. The control-volume technique based on the SIMPLE [28] algorithm was employed. The equations were solved using an algebraic multigrid solver [29, 30]. A double precision solver with a convergence criterion of 10^{-5} (relative tolerance) for all the field variables was used. The accuracy of the predictions was verified against the no-ribs case and the error was found to be less than 5% except at the entrance regions and transverse ribs (8%) where the current density is theoretically infinite. Simulations were also conducted to ensure that the results obtained were grid independent. Further details are provided elsewhere [22].

4 Results and discussion

The calculations correspond to a generic system without regard to which electrode is at limiting current. That is, we are interested in pure mass transfer effects. We allow the current density to be different on the two electrodes by letting them function independently and consider these results to be more general than if we had imposed charge conservation constraints. The application of these results to a net-PPER will require consideration as to which electrode would be limiting since limiting current conditions at both cathode and anode would not occur typically. In addition, since we calculate the local limiting current based on a centerline concentration (i.e., bulk concentration C_b) that is free to change in the axial or y-direction and on a velocity profile that depends on the geometry, the dimensionless results are independent of the reactions occurring at either

electrode. Thus, the results are applicable to either electrode and they allow comparison of limiting currents for different geometric configurations or placements of the electrode which may be limiting.

Figure 3 shows the predicted variation of the normalized local $\hat{i}^*_{noribs}$ along the flow direction ζ, based on the mass transfer correlation for the unobstructed channel with laminar flow, for a Newtonian liquid with constant properties [26]. The mass-transfer rate is infinite at the upstream edge of the electrode ($\zeta = 0$) where the fresh electrolyte is brought in contact with the electrode, consistent with the Lévêque solution. The current density $\hat{i}^*_{noribs}$decreases with increasing ζ since Θ_b decreases. Also shown on Fig. 3 is the percent difference between the numerical results and the Lévêque [8] solution. This error is acceptable, reflects the numerical limitations for the geometry under consideration and shows the limitation of the grid independence tests.

All the longitudinal ribs are taken to be of the same size. The transverse ribs also are the same size, but they differ from the dimensions of the longitudinal ribs (see Table 1).

4.1 Effect of longitudinal ribs

Consider the case where four equally spaced longitudinal ribs (there can be a maximum of 14 longitudinal ribs) are placed adjacent to electrode 2 and electrode 1 is suspended at a thickness of h_1 above the ribs. The total gap between the electrodes remains at $h_1 + h_2$. Figure 4 shows the variation of the normalized local current density i^* over the two individual electrodes. The white areas on the electrode 2 indicate the presence of longitudinal ribs, where the current density is zero. The current density decreases along the ζ direction since the driving force for mass transfer decreases along y. The effect of the longitudinal ribs can be viewed approximately as dividing the reactor into many smaller reactors of width equal to the spacing between adjacent longitudinal ribs (i.e., l_1 in Fig. 1b), The variation of the current density in the η direction on electrode 2 is minimal except in those regions which are under the influence of the ribs and those near the edges (i.e. $\eta = 0$ and $\eta = \frac{W}{L}$) since there is no flow along η for this velocity and geometry. Electrode 1 on the other hand, shows a different behavior due to the gap h_1 since the area of the region over the longitudinal ribs allows for a velocity distribution approaching a parabola which is influenced by the ribs within the space h_2. Thus there is a finite i^* in the η direction. Note that on electrode 1 there is "parabolic-like" profile between successive longitudinal ribs with a larger current density in the center of the spacing. There is some dispersion of this profile as one moves from electrode 2 to electrode 1 in the z direction. The limiting current density follows this change in the local velocity.

Also observed in Fig. 4 are the edge effects (highlighted by the dotted circles) for this velocity. That is, there is some "rounding" of the contours at $\eta = 0$ and $\eta = \frac{W}{L}$ since the geometry has a finite width and the CFD calculations capture the no-slip conditions. Similar rounding occurs at the interface between the first and last longitudinal ribs on electrode 2 as highlighted by the circle in Fig. 4.

Figure 5 shows a typical velocity profile when only the 4 longitudinal ribs featured in Fig. 4 are present. Two regions marked **A** and **B**, are of interest. Region **A** is the center of the flow region directly under the longitudinal ribs. Hence, region **A** is bounded by electrode 1 on the bottom and a longitudinal rib on the top. As expected, a parabolic-like profile in the y–z plane with the velocity being the maximum at the centre is observed. However, in

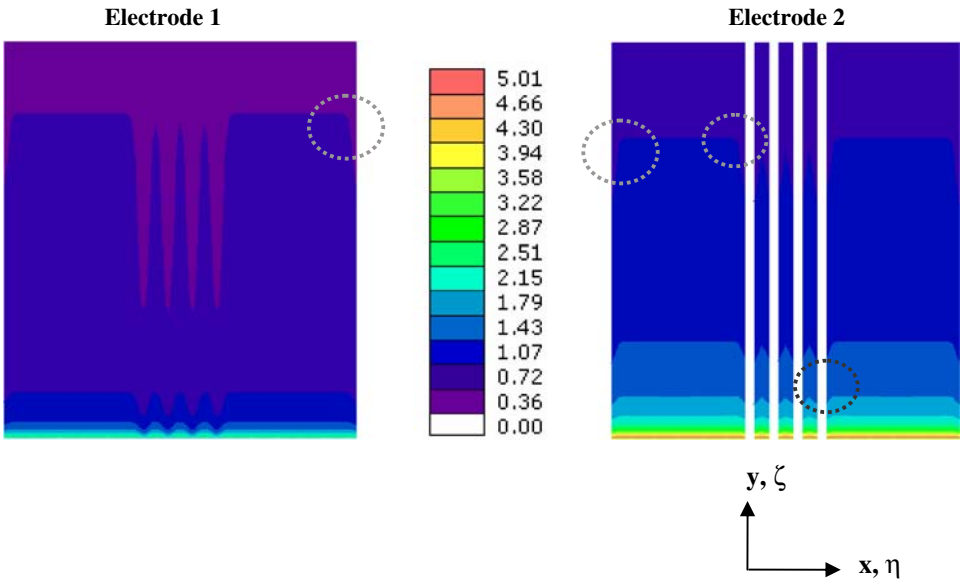

Fig. 4 Distribution of the normalized local current densityi^* for the case of 4 longitudinal ribs (max 14). No transverse ribs are featured. The circles indicate regions where edge/rib effects are observed

the z–x plane the velocity profile shows a different pattern. The velocity at the centre of region **A** is observed to be the lowest. As we move from region **A** along the x-direction the velocity increases and attains a maximum at region **B**. Thereafter, it decreases and attains a minimum in the next region **A**. This pattern repeats along the x-direction. Region **B**, is bounded by the electrodes and shows a parabolic-like profile in both the planes namely y–z and z–x but with a much higher average velocity. Thus in region **A**, the rate of mass transfer would be much lower than that in region **B**. Since the average velocity in the y-direction of region **A** $\bar{v}_A$ is also much lower than that of the no-ribs case (i.e., $\bar{v}_{noribs} = 1 \times 10^{-2}$ m s^{-1}), the mass transfer in the region **A**, would be much lower than the no-ribs case. On the other hand, in region **B,** average velocity in the y-direction $\bar{v}_B$, is much higher than $\bar{v}_{noribs}$ and the mass transfer would be higher than the no-ribs case. In other words, region **A** would show a negative deviation from the Lévêque solution while region **B** is expected would show a positive deviation.

Figure 6 shows the variation of Δ_1 and Δ_2 along η over electrodes 1 and 2, at two different values of ζ (0.06 and 0.21). A family of such curves provides an idea of the variation of Δ over the two electrodes in both ζ and η directions. Fig. 6a and b, both show four regions which are considerably different in behavior. Near the edges, Δ monotonically goes to zero due to no slip conditions and there can be no mass transfer in both the no-ribs and the ribbed cases. Hence, the respective values of the current density go to zero and any difference between them, Δ, also goes to zero. However, in the regions far away from the ribs and edges, Δ is a constant for a given number of longitudinal ribs n_l since, the velocity profile and the mass transfer conditions are invariant in those regions. The value of Δ falls off only near the edges and ribs. Similar to the edges, the regions immediately surrounding the longitudinal ribs are places where the insulating ribs meet the solution. In the regions directly under the ribs (region **A**), the value of Δ is negative showing that the values of current density are significantly different from the values of the no-ribs case. However, the regions between any two successive longitudinal ribs (region **B**) are available for mass transfer and hence Δ is non-zero in that region. In addition, it is observed that Δ is high in these regions (region **B**), indicating that the results are consistent with the flow field in Fig. 5.

While both the electrodes show the above behavior, there are some important differences between them. Figure 6a shows that at $\zeta = 0.06$ in electrode 1, Δ_1 shows a minimum of -42% whereas the corresponding value of Δ_2 shown in Fig. 6b at electrode 2 is -166%. Both these

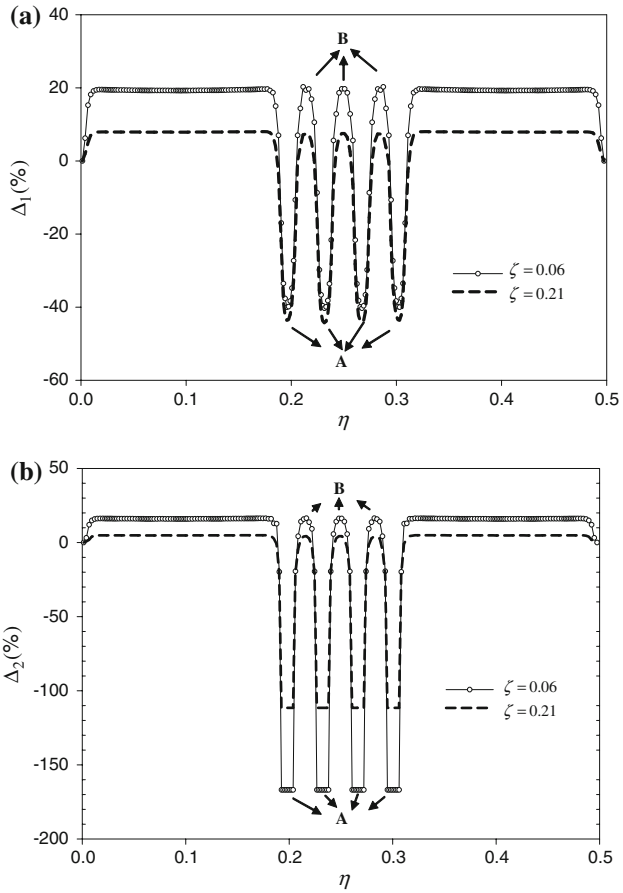

Fig. 6 Variation of the Δ_1 and Δ_2 along η, at two locations of ζ (0.06 and 0.21) for the case of 4 longitudinal ribs shown in Figs. 4, 5. Note that the regions marked **A** and **B** in Fig. 5 have been featured in this graph for convenience. All the positive peak regions correspond to region **B** and all the negative peak regions correspond to region A

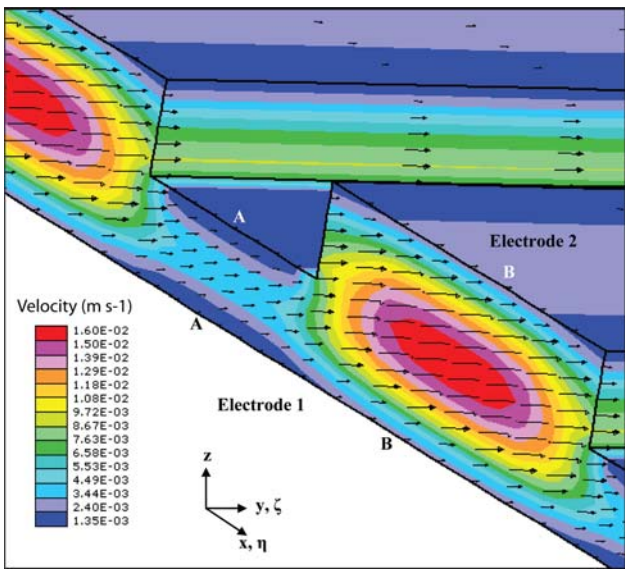

Fig. 5 Flow field distribution when only longitudinal ribs are present (refer Fig. 4). Regions **A** and **B** are the centers of ribbed and non-ribbed regions respectively

values correspond to region **A** of Fig. 5. This huge difference between Δ_1 and Δ_2 is explained by recalling the definition of Δ in Eq. 14. The value of current density at the ribs itself is zero. Hence at those places, Δ_2 would simply be the ratio of the local current density i_{noribs}, and the average current density for the no-ribs case i_{avg_noribs}. This value of Δ_2 in the region **A** shown in Fig. 6b is consistent with the Lévêque solution which shows a value of 1.66 for the ratio at $\zeta = 0.06$.

On the other hand, at electrode 1, the local current density i has a non-zero value and Δ_1 retains the original physical meaning of being the deviation from the no-ribs case. Interestingly, the maximum value of Δ_1 attained in the rib-free region is equal to the maximum value of Δ_1 in between successive longitudinal ribs. The smooth profiles also indicate that the width of the live cell spacing between any two ribs is not affected by the grid size. In Fig. 6b, Δ_2 also shows the same behavior in the region **B**, although the maxima of Δ_2 are somewhat lower ($\approx$5%) than the corresponding maxima of Δ_1. This effect is due to the parabolic-like velocity profile. Figure 6a and b also show that, for a given electrode the extremes shift to lower values along ζ since the conversion in the reactor increases along ζ and the driving force for mass transfer decreases. Hence the current density for both the no-ribs and the ribbed cases decreases. As the current density approaches zero along the axial direction, the difference between the no-ribs and the ribbed cases gets smaller and the graphs of Δ vs. η shift progressively to lower values.

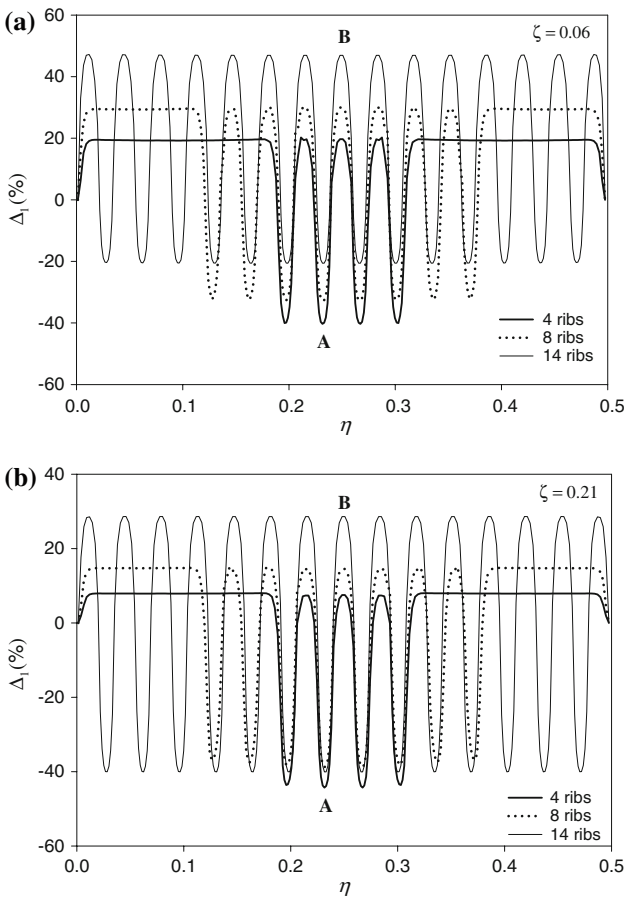

Fig. 7 Variation of Δ_1 along η for the case of 4, 8, and 14 longitudinal ribs and no transverse ribs at two different locations of ζ (0.06 and 0.21) for the simulation presented in Figs. 4, 5. Note that the regions marked **A** and **B** in Fig. 5 have been featured in this graph for convenience All the positive peak regions correspond to region B and all the negative peak regions correspond to region **A**

Figure 7 shows the effect of n_l on the variation of Δ_1 along η for two different locations of ζ (0.06 and 0.21). Two distinct effects can be observed: (1) at a given ζ, as n_l increases, the maximums (and minimums) of Δ_1 shift in a positive direction (2) along ζ, as n_l increases, the difference between the maximums (and minimums) of decreases. That is, the quantities $\left(\Delta_1^{\max}(14) - \Delta_1^{\max}(8)\right)$ and $\left(\Delta_1^{\min}(14) - \Delta_1^{\min}(8)\right)$ decrease where the numbers in the braces denote the number of longitudinal ribs. The first effect is observed because, as n_l increases, the number of constricted regions through which the fluid flows also increases. In these constricted regions which correspond to region **A** in Fig. 5, the average velocity $\bar{v}_A$ is much less than $\bar{v}_{norbis}$. However, the values of maximum axial velocity which occurs at the center of the region **A**, are 3.44×10^{-3}, 3.88×10^{-3}, and 4.33×10^{-3} m s^{-1} for 4, 8, and 14 longitudinal ribs respectively indicate that $\bar{v}_A$ increases as n_l increases. This is expected since as n_l increases, the cross section area of the flow decreases and the average velocity $\bar{v}_A$ increases. Hence, the local current density in region **A**, increases with increasing n_l and consequently Δ_1 decreases. In region **B** also, a similar effect is observed, but $\bar{v}_B$is much higher than $\bar{v}_{norbis}$. The values of maximum axial velocity which occurs at the centre of the region **B**, are 1.6×10^{-2}, 1.73×10^{-2}, and 2.0×10^{-2} m s^{-1} for 4, 8, and 14 longitudinal ribs respectively indicating that the $\bar{v}_B$ also increases as n_l increases. Thus, Δ_1 becomes more positive as n_l increases. The rate of decrease of Δ_1 along ζ increases with n_l. For example, the highest rate of decrease is observed for the case of 14 longitudinal ribs (from 48 to 28% in the maxima and from -20 to -40% in the minima), and the lowest rate of decrease occurs for 4 longitudinal ribs (from 17 to 7% in maxima and from -40 to -43% in the minima). Both the regions **A** and **B** of Fig. 5 show an increase in the average velocity which leads to higher conversion and a lower value of Δ_1. The second effect is due mainly to the decrease in conversion since the velocity profile is invariant along ζ for the case featuring longitudinal ribs only. As the conversion decreases, the extremes of Δ_1 start shifting in the negative direction. Hence, in region **B** the difference between the no-ribs and the ribbed cases starts decreasing. However, in region **A**, the low value of $\bar{v}_A$ leads to considerably larger negative value of Δ_1.

4.2 Effect of transverse ribs

Figure 8 shows the distribution of normalized local current density i^* for two transverse ribs placed at two different locations of ζ when the spacing between the two ribs is maintained at l_2. In arrangement 1 the first rib is placed at $\zeta = \frac{l_2}{L} = 0.0214$ and in arrangement 2 the first rib placed at$\zeta = 0.23$. By first rib, we denote the transverse rib which is closer to the entrance of the reactor. Unlike the longitudinal ribs, the transverse ribs constrain and expand the flow path (see Fig. 9) thus altering the local rates of mass transfer drastically. In Fig. 8 the contours along the η direction change only in the edge regions marked by the dotted circles as expected. At a given ζ, the mass transfer in the edge regions is lower than that in the other regions. The values of i^* in these encircled regions can be as low as 33% below the local average $\hat{i}^*$ for the given reactor. However, the fraction of the total area influenced by the edges is less than 4% since the edge effects are 0.7% of the local average $\hat{i}^*$ for this case. Hence, the deviation from the no-ribs case can be understood by plotting $\hat{\Delta}$, a value of Δ

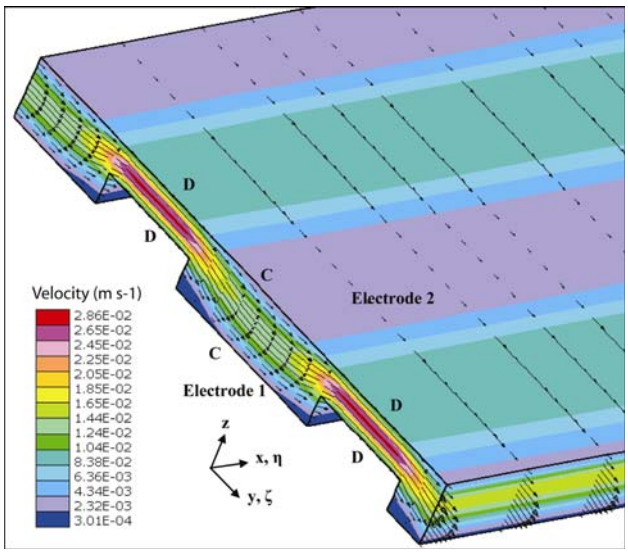

Fig. 9 Flow field distribution when only 2 transverse ribs are present as shown in arrangements 1 and 2 given in Fig. 8. Regions **D** and **C** are the centers of the ribbed and the non-ribbed regions respectively. Note that no longitudinal ribs are featured

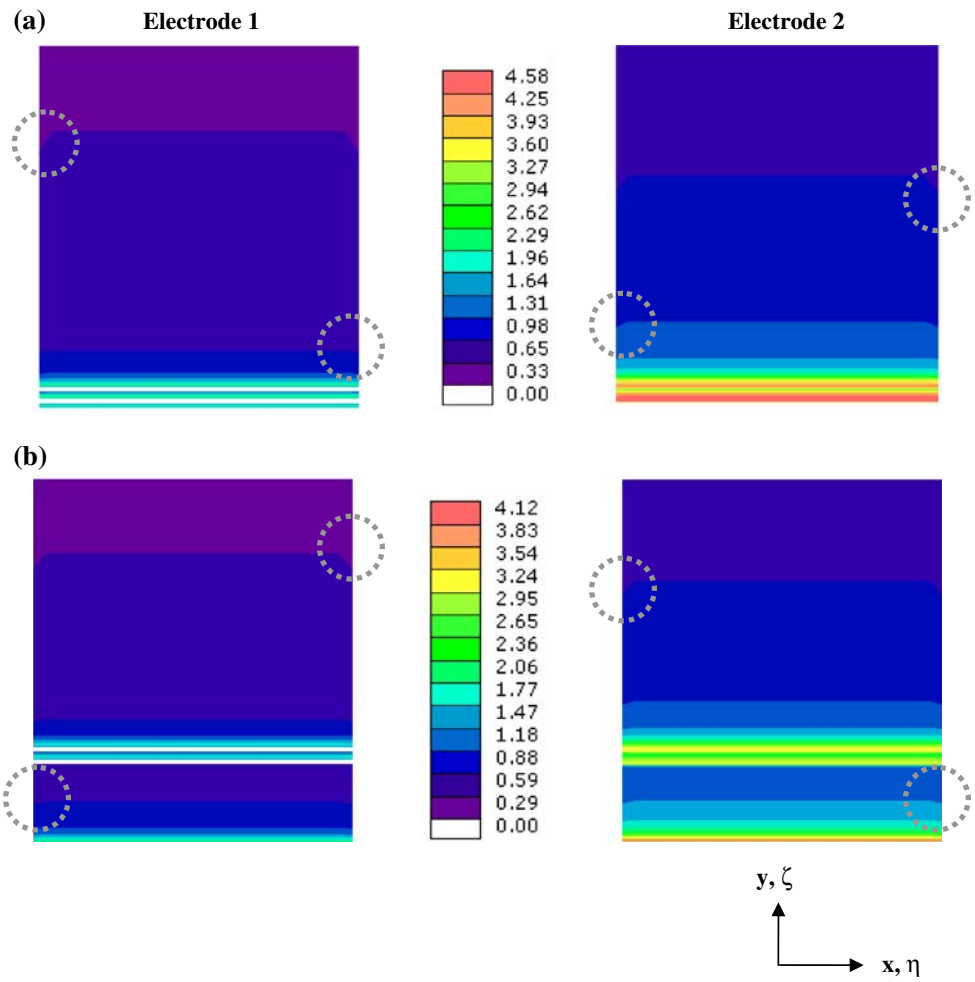

Fig. 8 Distribution of the normalized local current density i^* for two different positioning (non-dimensional) of 2 transverse ribs, **(a)** positioning 1—$\zeta = \frac{l_2}{L} = 0.0214$—arrangement 1 **(b)** positioning 2—$\zeta = \frac{6(w_2+l_2)+l_2}{L} = 0.23$—arrangement 2. The non-dimensional spacing between the two ribs in the arrangements is $\frac{l_2}{L}$ No longitudinal ribs are featured. The circles indicate the regions where edge effects are observed

averaged in the η direction, as a function of ζ as shown in Fig. 10.

Figure 10 shows the variation of $\hat{\Delta}$ along ζ on the two electrodes, for the arrangements 1 and 2 in Fig. 8. Figure 10a and b, both show very high deviations from the no-ribs case, in the regions where transverse ribs are encountered. However, these deviations must be interpreted with caution. Figure 3 shows that the numerical solution deviates from the Lévêque solution as ζ decreases. In other words, the uncertainty in predicting the values of current density is highest at the entrance where the rate of mass transfer is theoretically infinite. A similar situation is encountered at when fluid meets a transverse rib. For example, in the entrance region of the reactor, for $\zeta \approx 0.01$ the difference between the numerical and the theoretical Lévêque solutions can be as high as 8%. In Fig. 4. For $\zeta \approx 0.025$ the difference is close to 7%. The transverse ribs induce an "entrance effect" when the fluid flows from region **D** to **C** by blocking some mass-transfer area (see Fig. 9). The non-dimensional width of a transverse rib $\frac{w_2}{L}$ is 0.013 and the non-dimensional live-cell spacing between the two transverse ribs, $\frac{l_2}{L}$ is 0.026. These values are comparable to the values of ζ at the entrance region, where a considerable uncertainty exists in predicting the values of i^*, as shown in Fig. 3. Computations performed over such small regions near the transverse rib regions, also suffer from the same uncertainty in predicting the values in these regions. The accuracy may be improved by using a highly refined grid in these regions which however is limited by the computational resources. The current model employs more than 800,000 computational cells, which is relatively large. Hence, the high values of $\hat{\Delta}$ observed in Fig. 10 must be used keeping in mind the margin of error introduced due to grid limitations.

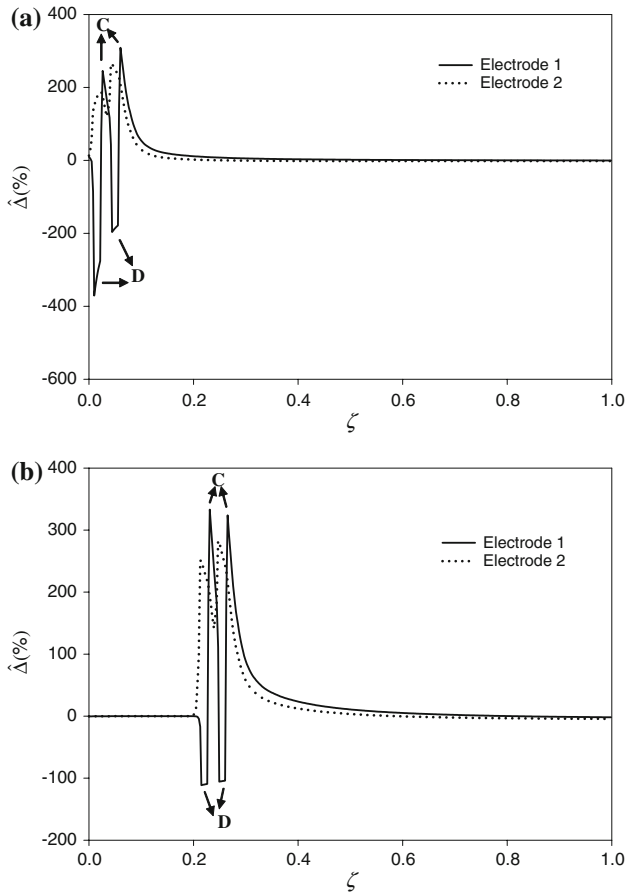

Fig. 10 Variation of $\hat{\Delta}$ along ζ for electrodes 1 and 2 for two transverse ribs featured in **(a)** arrangement 1 and **(b)** arrangement 2 of Figs. 8, 9. Note that no longitudinal ribs are featured. Regions marked **C** and **D** in Fig. 9 have been featured in this graph for convenience. All the positive peak regions correspond to region **C** and all the negative peak regions correspond to region **D** shown in Fig. 9

At electrode 1, in the regions where transverse ribs are present, the value of $\hat{\Delta}$ reduces to $\hat{i}^*$ (refer to Eq. 14) since the local current density is zero. However, at electrode 2, the area for mass transfer is still available and $\hat{\Delta}$ retains the original physical meaning of being the measure of deviation from the no-ribs case. Figure 9 shows that the average velocity of region **D** is significantly higher than that of region **C**. Hence, electrode 2 must show a higher current density in region **D** compared to region **C**. This is illustrated by the dotted lines in Fig. 10 which decrease in region **C**, although maintaining a positive value. Figure 10b shows the "entrance effect" that the transverse ribs induce, much more clearly. As the fluid enters the reactor, the influence of the transverse ribs is not immediately felt and the flow field is similar to the case with no-ribs. Hence $\hat{\Delta} = 0$, in this region. However, when a transverse rib is encountered, the flow field changes drastically (see Fig. 9) and the rate of mass transfer is altered highly at both the electrodes. The electrode 1, shows a $\hat{\Delta}$ value corresponding to the local $\hat{i}^*$ and electrode 2 shows a very highly positive value for $\hat{\Delta}$ since the average velocity has increased. Beyond the rib region, the flow field starts developing and after some distance along ζ, becomes identical to the fully developed flow field at the entrance of the reactor. Hence, the graph of $\hat{\Delta}$ vs. ζ falls of asymptotically towards zero since $\hat{i}^*$ and $\hat{i}^*_{noribs}$ both go to zero along ζ.

Figure 11 shows arrangements 3 and 4 of two transverse ribs, with different spacing between them. Together with the arrangement 2, presented in Fig. 8b, they help understand the effect of the spacing between the transverse ribs on the current density distribution over electrodes 1 and 2. As the spacing is increased, the rate of change of contours along ζ decreases. This effect is due to the influence of the downstream rib on the upstream velocity profile in between the ribs. The larger the spacing between the ribs, the lower the influence of the downstream rib and the higher the similarity to the no-ribs case. This effect is made clearer by the asymptotic behavior in Fig. 12. The regions marked

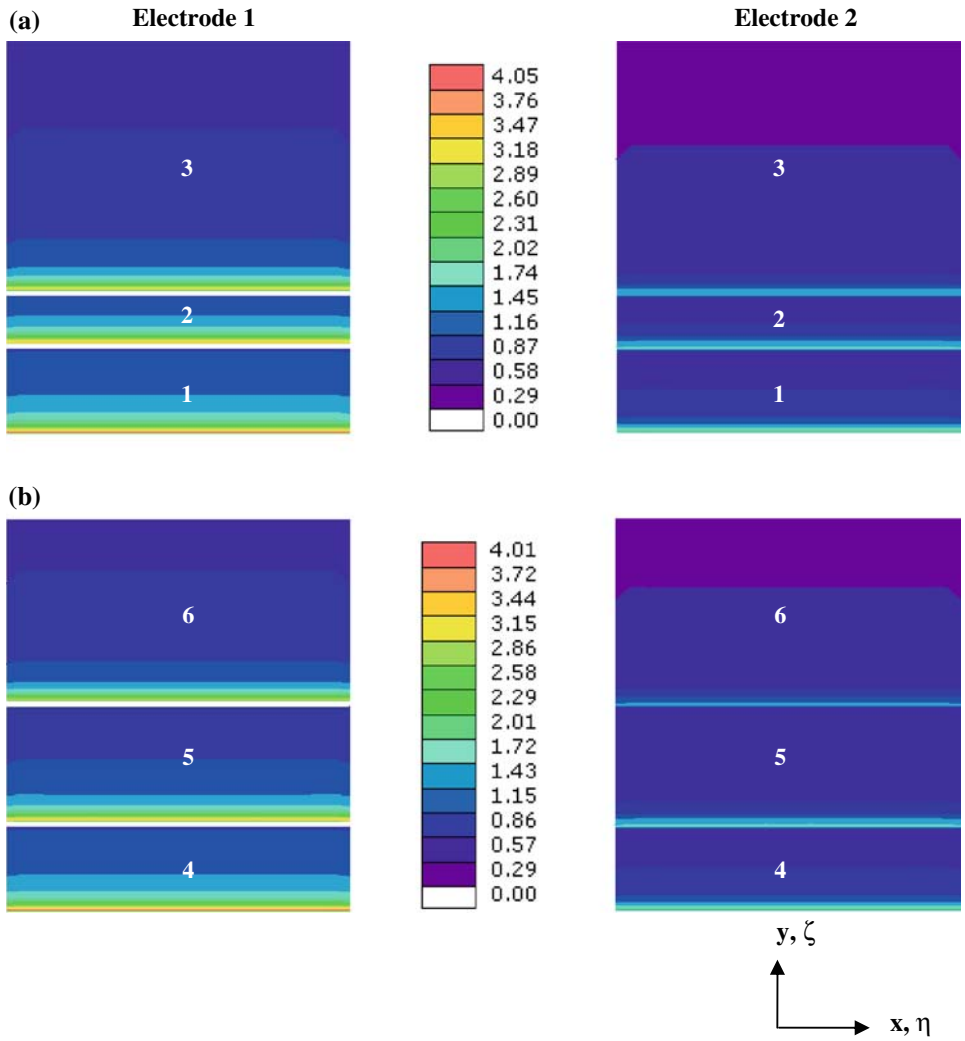

Fig. 11 Distribution of the normalized local current densityi^* for different spacing of 2 transverse ribs: (**a**) arrangement-3-*spacing* $= \frac{3(w_2+l_2)+l_2}{L} = 0.12$ (**b**) arrangement-4 *spacing* $= \frac{8(w_2+l_2)+l_2}{L} = 0.3$. The first rib is placed at $\zeta = \frac{6(w_2+l_2)+l_2}{L} = 0.23$ in both the arrangements. Note that no longitudinal ribs are featured

1–6 in Fig. 11 are marked in Fig. 12 also. The profile of $\hat{\Delta}$ along ζ in the regions 1 and 4 are clearly identical. Region 2 shows a much greater rate of decrease of $\hat{\Delta}$ along ζ than region 5. Once again, since the geometry of regions 3 and 6 are similar to the no-ribs case, $\hat{\Delta}$ asymptotically approaches zero. Thus, a transverse rib can be perceived as a local disturbance in the primary flow direction which fades along ζ unless enhanced by another transverse rib in the path of the fluid. Part II discusses the combined effects and the enhancement obtained in various cases.

5 Conclusions

The effect of the net-geometry on limiting current density distribution in a parallel plate channel was presented. The net affects the velocity profiles significantly, resulting in zones of high, low, and zero mass transfer. The individual effects of the longitudinal and the transverse ribs on the current density distribution were presented. The dependence of current density on the type, positioning, spacing and number of ribs was documented. The longitudinal ribs decrease the local current density at the electrode that is not in contact. However, in the space between two adjacent longitudinal ribs, the local current density increases, although the current density is zero on the top of the ribs themselves. A deviation of −40% was observed for a system of 4 longitudinal ribs and no transverse ribs at the non-dimensional axial position 0.06. Transverse ribs affect the current distribution far more significantly than the longitudinal ribs. They increase the local current density to very high values at the electrode that is not in contact e.g. the deviation at the non-dimensional axial position 0.06 was approximately 250%. The current density, however,

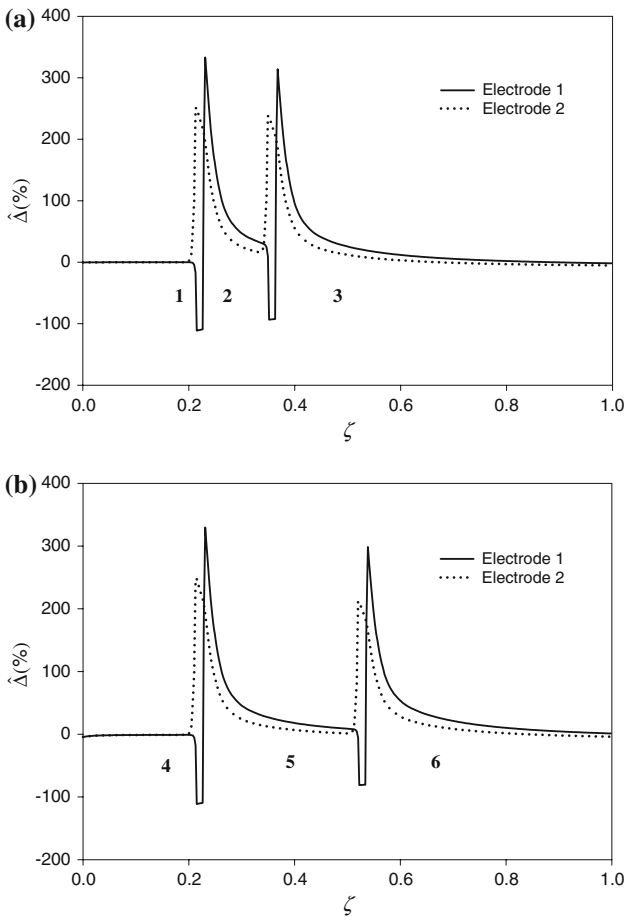

Fig. 12 Variation of $\hat{\Delta}$ along ζ for electrodes 1 and 2 for **(a)** arrangement 3 and **(b)** arrangement 4 shown in Fig. 11. Note that no longitudinal ribs are featured. Regions **1–6**, shown in Fig. 11 are featured here for convenience

falls along the flow direction as it exits the transverse-ribs region. The validity of the solutions was ascertained by simulating the no-ribs case and verifying it against a correlation in the literature. The behaviour of the ribbed systems was presented as percent deviation from the no-ribs case which could be used as a tool for the optimal design of the system. The numerical results have a less than 5% error for the no-ribs case except at the entrance of the channel and at the transverse ribs where the error is around 8%. All the results are for a net with a spacing of 0.94×10^{-3} m.

Acknowledgement The authors acknowledge Dr. Sirivatch Shimpalee of University of South Carolina for his useful inputs in the CFD calculations of this paper.

References

1. Bain M, Raible M, White RE (1982) J Electrochem Soc 129:C119
2. White RE, Bain M, Raible M (1983) J Electrochem Soc 130:1037
3. Nguyen TV, Walton CW, White RE et al (1986) J Electrochem Soc 133:81
4. Prasad S, Weidner JW, Farell AE (1995) J Electrochem Soc 142:3815
5. Parrish WR, Newman J (1969) J Electrochem Soc 116:169
6. Parrish WR, Newman J (1970) J Electrochem Soc 117:43
7. Edwards V, Newman J (1987) J Electrochem Soc 134:1181
8. Newman JS (1991) Electrochemical systems. Prentice Hall, Englewood Cliffs
9. Fan D, White RE (1991) J Electrochem Soc 138:1688
10. Brodrecht DJ, Rusek JJ (2003) Appl Energy 74:113
11. Popovich NA, Govind R (2002) J Power Sources 112:36
12. Bessette RR, Cichon JM, Dischert DW et al (1999) J Power Sources 80:248
13. Dow EG, Bessette RR, Seeback GL et al (1997) J Power Sources 65:207
14. Hasvold O, Johansen KH, Mollestad O et al (1999) J Power Sources 80:254
15. Young TJ, Vafai K (1998) Int J Heat Mass Transfer 41:3131
16. Bhavnani SH, Bergles AE (1990) Int J Heat Mass Transfer 33:965
17. Tanda G (1997) Int J Heat Mass Transfer 40:2173
18. Song TH (2000) Numer Heat Transf Part A-Appl 38:491
19. Wragg AA, Leontaritis AA (1997) Chem Eng J 66:1
20. Oduoza CF, Wragg AA (2002) Chem Eng J 85:119
21. Oduoza CF, Wragg AA (2000) J Appl Electrochem 30:1439
22. Venkatraman M (2006) Models for mass transfer effects in semi-fuel cells and for a Silver-Zinc battery. Dissertation, University of South Carolina, Columbia
23. Venkatraman M, Shimpalee S, Van Zee JW (2009) Effect of net geometry on the Nusselt Number distribution for channel flow. Numer Heat Transf
24. Littauer EL, Tsai KC (1979) J Electrochem Soc 126:1924
25. Chu D, Savinell RF (1991) Electrochim Acta 36:1631
26. Bird RB, Stewart WE, Lightfoot EN (2002) Transport phenomena. John Wiley &Sons (Asia) Pte Ltd, Singapore
27. Lévêque J (1928) Ann Mines (series 12). 13:201,305,381
28. Patankar SV (1980) Numerical heat transfer and fluid flow. Hemisphere, New York
29. Tannehill JC, Anderson DA, Pletcher RH (1997) Computational fluid mechanics and heat transfer. Taylor & Francis, London
30. STAR-CD, "User Guide, v3.10". Computational Dynamics Limited